

Spectral Indicators of Piezomagnetically Induced Symmetry Breaking in Altermagnets

N. Sasabe,¹ H. Koizumi,² Y. Ishii,¹ and Y. Yamasaki^{1,3,4}

¹Center for Basic Research on Materials (CBRM),

National Institute for Materials Science (NIMS), Tsukuba, Ibaraki, 305-0047, Japan

²Department of Applied Physics, University of Tsukuba, Tsukuba, Ibaraki 305-8573, Japan

³International Center for Synchrotron Radiation Innovation Smart, Tohoku University, Sendai 980-8577, Japan

⁴Center for Emergent Matter Science (CEMS), RIKEN, Wako 351-0198, Japan

Recent developments in the multipole reformulation of X-ray absorption spectroscopy (XAS) have provided a unified framework to describe magnetic and orbital responses in terms of ferroic multipole order parameters. X-ray magnetic circular dichroism (XMCD) is known to probe spin, orbital, and anisotropic magnetic dipole (AMD) moments. Its applications to altermagnets and noncollinear antiferromagnets have revealed that the XMCD response is often governed by the ferroic states of the AMD in the photo-excited states rather than by conventional magnetic dipoles in the ground states. In this work, we extend the multipole-based analysis to X-ray magnetic linear dichroism (XMLD) and demonstrate that XMLD in altermagnets can be understood as a manifestation of piezomagnetic effects: linear couplings between magnetic dipole and electric quadrupole moments. Using symmetry analysis combined with exact diagonalization calculations of $L_{2,3}$ -edge XAS, we systematically investigate representative altermagnets, including α -MnTe, MnF₂, and CrSb. We show that the ferroic ordering of higher-rank magnetic multipoles, particularly spinful magnetic octupoles, gives rise to characteristic field-odd XMLD signals that directly reflect the underlying piezomagnetic response tensors allowed by magnetic point-group symmetry. Furthermore, we discuss XMCD signals induced by piezomagnetic effects, in which strain generates magnetic dipole moments. Our results establish XMLD and XMCD as element-specific probes of magnetoelastic multipole order in altermagnets and provide a general symmetry-based pathway to identify hidden ferroic multipoles and strain-controllable spin phenomena beyond conventional ferromagnetism.

INTRODUCTION

Altermagnets

Magnetic materials have long been classified into ferromagnets, ferrimagnets, and antiferromagnets based on net magnetization and magnetic ordering [1–4]. In conventional *collinear* antiferromagnets, the combination of spatial inversion and time-reversal symmetry preserves spin degeneracy, thereby forbidding momentum-dependent spin splitting [5–9]. This classification has been broadened by the theoretical prediction of a new class of magnets termed *altermagnets*: collinear magnets with zero net magnetization yet with spin-split electronic bands [10–12]. The spin splitting does not originate from spin-orbit coupling (SOC); rather, it is enforced by magnetic space-group symmetries that act differently on spin-up and spin-down channels in momentum space [13]. Thus, these systems break global spin degeneracy while preserving a joint symmetry of crystal operations with time reversal, allowing momentum-dependent spin polarization without net magnetization.

In antiferromagnets, the symmetry of the magnetic multipole order plays a central role in determining observable macroscopic responses. For example, in systems such as Mn₃Sn and the g -wave altermagnet MnTe, whose magnetic structures effectively possess magnetic dipole symmetry, phenomena analogous to those in ferromagnets have been observed or theoretically anticipated, including X-ray magnetic circular dichroism (XMCD), the magneto-optical Kerr effect (MOKE), and the anoma-

lous Hall effect (AHE) [14–17]. In these materials, the broken time-reversal symmetry combined with appropriate crystal symmetry enables finite Berry curvature and transverse transport responses despite the absence of net magnetization. By contrast, d - and g -wave altermagnets with magnetic octupole symmetry are characterized by momentum-odd spin splitting without net Berry curvature, thereby suppressing the conventional AHE while still permitting unconventional responses [18–20]. In particular, higher-order altermagnetic states, such as g -wave and f -wave types, are predicted to host transverse spin currents even in the absence of SOC [21–23], as well as symmetry-allowed piezomagnetic and magnetoelastic effects that directly reflect the multipolar nature of the underlying spin splitting [24–26]. These features highlight a qualitative distinction between dipolar antiferromagnets, which can mimic ferromagnetic responses, and higher-rank altermagnets, where transport and magnetoelastic phenomena are governed by multipolar symmetry rather than Berry-curvature-driven mechanisms.

Spinless and spinful magnetic multipoles

From a symmetry viewpoint, each magnetic point group corresponds to a definite pattern of spatial and time-reversal symmetry breaking that can be identified with a leading ferroic magnetic multipole (dipole, quadrupole, octupole, *etc.*) transforming as the same irreducible representation [27–32]. This perspective unifies complex antiferromagnetic orders as manifestations

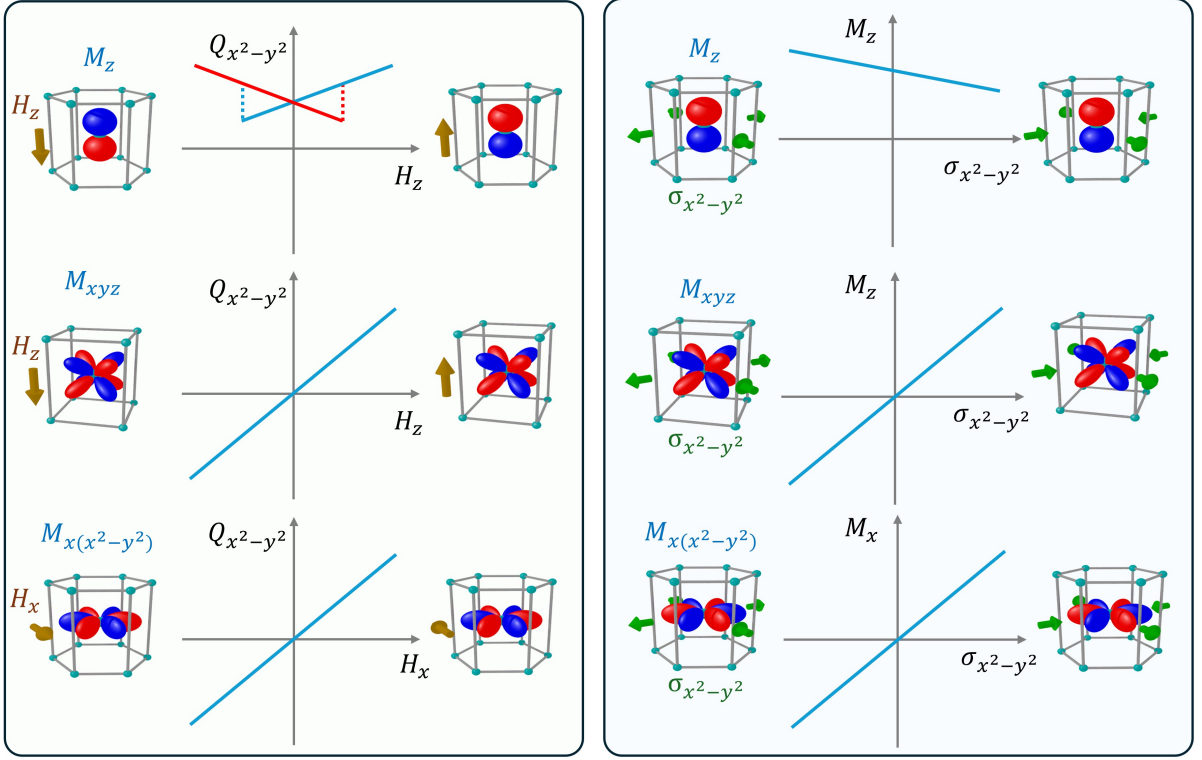


FIG. 1. Schematic illustration of electronic and magnetic response functions in altermagnetic systems. (Left) Response of the electric quadrupole moment $Q_{x^2-y^2}$ to an external magnetic field H , where brown arrows indicate the direction of the applied magnetic field. In an altermagnet possessing magnetic dipole symmetry M_z , the application of a magnetic field induces an electric quadrupole moment through the coupling between M_z and the field. At sufficiently high magnetic fields, however, the magnetic dipole M_z can reverse its orientation. As a result, the induced quadrupole response becomes symmetric (even) with respect to the magnetic field H_z . In contrast, if magnetic octupoles, M_{xyz} and $M_{x(x^2-y^2)}$, do not directly flip with the magnetic field, they lead to antisymmetric (odd) linear responses in $Q_{x^2-y^2}$ as a function of H_z or H_x , respectively. (Right) Response of the magnetic dipole to external symmetric strain $\sigma_{x^2-y^2}$, with green arrows indicating the direction of the applied strain. Each panel illustrates the emergence of magnetic moments under corresponding multipolar orderings. Similar to the magnetic field response, the induced magnetic dipole is governed by the linear coupling between the applied strain and the pre-existing multipolar symmetry of the d -wave and g -wave altermagnetic states.

of ferroic multipoles and provides a robust route to predict response tensors purely from symmetry.

Multipole expansions offer a systematic description of charge and magnetic distributions [33, 34]. Beyond the conventional electric (\mathbf{Q}) and magnetic (\mathbf{M}) multipoles, the *complete* basis incorporates electric toroidal (\mathbf{G}) and magnetic toroidal (\mathbf{T}) multipoles and their spinful counterparts, obtained by coupling orbital tensors with spin degrees of freedom [30, 32]. Let $\hat{X}_{\ell m}^{(\text{orb})}$ and $\hat{\sigma}_{s,n}$ denote a spinless orbital multipole ($X \in \{Q, M, T, G\}$) and a Pauli matrix, respectively. The spinless ($s = 0$) and spinful ($s = 1$) operators are constructed via angular-momentum coupling as

$$\hat{X}_{\ell m}^{(s,k)} = i^{s+k} \sum_{n=-s}^s C_{\ell+k, m-n; s n}^{\ell m} \hat{X}_{\ell+k, m-n}^{(\text{orb})} \hat{\sigma}_{s n}, \quad (1)$$

where $C_{l_1, m_1; l_2, m_2}^{l, m}$ is the Clebsch-Gordan coefficient, $k \in \{-s, \dots, s\}$, $\hat{\sigma}_0 = \hat{\sigma}_z$, $\hat{\sigma}_{10} = \hat{\sigma}_z$, $\hat{\sigma}_{1, \pm 1} = \mp(\hat{\sigma}_x \pm i\hat{\sigma}_y)/\sqrt{2}$.

Since spin is an axial vector and is odd under time reversal, the spinful $\hat{X}_{\ell m}^{(1,k)}$ possesses transformation properties opposite in time reversal parity to the orbital tensor with which it couples. In d -electron systems, for example, a spinful magnetic multipole may combine orbital tensors of different spatial parities, enabling higher-rank magnetic octupoles that are ferroic even in centrosymmetric antiferromagnets [24].

Piezomagnetic Effects

The piezomagnetic couplings describe the fundamental coupling between magnetic and elastic degrees of freedom, encompassing phenomena in which magnetic order and lattice deformation mutually influence each other [35–38]. From a phenomenological viewpoint, this coupling manifests itself in two distinct responses: the direct piezomagnetic effect (magnetostriction) and its inverse

effect. The total strain response ε_{jk} of a magnetic system under an external magnetic field \mathbf{H} can be systematically expressed as

$$\varepsilon_{jk} = \Lambda_{i;jk}^T H_i + N_{jk;mn} H_m H_n, \quad (2)$$

where the first and second terms represent the linear piezomagnetic and quadratic magnetostrictive contributions, respectively. The quadratic term, magnetostriction, is a universal feature of magnetic materials and is characterized by a rank-4 tensor $N_{jk;mn}$. Since it depends on even powers of the magnetic field, the induced strain is invariant under field reversal. In contrast, the linear term describes the inverse piezomagnetic effect, governed by the rank-3 tensor $\Lambda_{i;jk}$. This coupling is odd under time reversal and therefore requires magnetic order. The corresponding direct piezomagnetic effect, namely the induction of magnetization m_i by external strain ε_{jk} , is expressed as

$$m_i = \Lambda_{i;jk} \varepsilon_{jk}. \quad (3)$$

Unlike the piezoelectric effect, which requires broken inversion symmetry, the piezomagnetic effect is symmetry-allowed even in certain centrosymmetric crystals, provided that time-reversal symmetry is broken by magnetic ordering [39–41].

From a microscopic perspective, the inverse piezomagnetic effect can be interpreted as a magnetic-field-induced modification of electric quadrupole moments Q_{2m} . These induced quadrupoles couple to the lattice via electron-lattice interactions, giving rise to a macroscopic strain response [42]. Since lattice strain and stress transform as rank-2 symmetric tensors, they can naturally be identified with electric quadrupole degrees of freedom. This observation provides a direct link between piezomagnetic responses and magnetic multipole order. Symmetry analysis shows that the piezomagnetic effect is allowed in systems hosting ordered magnetic dipoles M_{1m} , magnetic toroidal quadrupoles T_{2m} , or magnetic octupoles M_{3m} [28, 43, 44]. Although magnetostriction may also occur in antiferromagnets, it can be distinguished from the piezomagnetic effect by its even parity with respect to magnetic-field reversal [45–48].

PIEZOMAGNETIC EFFECTS IN ALTERMAGNETS

In this work, we focus on altermagnets and analyze their magnetoelastic responses within the framework of magnetic multipole theory. Since our primary interest is the spectroscopic response in X-ray absorption spectroscopy (XAS), we restrict the discussion to atomic magnetic multipoles rather than augmented (extended) multipoles. In other words, we focus only on those components of the extended multipoles that can be mapped onto the atomic picture and are spectroscopically observable, namely the electronic orders of magnetic dipoles, electric quadrupoles, and magnetic octupoles.

The emergence of piezomagnetic and inverse piezomagnetic effects associated with various magnetic multipole orders can be systematically formulated using the spherical harmonics representation [49]. Within this framework, the coupling between magnetic multipoles, external fields, and strain is governed by angular momentum selection rules encoded in Clebsch-Gordan coefficients:

$$Q_{2m} = \sum_{n,m'} (\alpha C_{1m';1n}^{2m} M_{1m'} + \beta C_{3m';1n}^{2m} M_{3m'}) H_{1n}, \quad (4)$$

$$M_{1m} = \sum_{n,m'} (\gamma C_{1m';2n}^{1m} M_{1m'} + \delta C_{3m';2n}^{1m} M_{3m'}) \sigma_{2n}. \quad (5)$$

Here, Q_{2m} , M_{1m} , and M_{3m} denote the electric quadrupole, magnetic dipole, and magnetic octupole moments, respectively. The external magnetic field H_{1n} and the symmetric strain tensor σ_{2n} are treated as rank-1 and rank-2 spherical tensors, respectively. The Clebsch-Gordan coefficients $C_{l_1 m_1; l_2 m_2}^{l m}$ impose strict symmetry constraints on the allowed couplings. Importantly, a given magnetoelastic response is symmetry-allowed only when the corresponding Clebsch-Gordan coefficient is nonzero. This condition directly connects macroscopic piezomagnetic responses to the underlying ferroic magnetic multipole order and the angular momentum structure of the electronic degrees of freedom.

The physical implications of Eqs. (4) and (5) are schematically summarized in Fig. 1, and their relation to Eqs. (2) and (3) is discussed as follows. The figure visualizes how the angular-momentum selection rules encoded in the Clebsch-Gordan coefficients determine the parity and linearity of magnetoelastic responses for different primary multipole orders. We first consider Eq. (4), which corresponds to the inverse piezomagnetic (magnetostriction) effect expressed in Eq. (2), namely the lattice deformation ε_{jk} induced by an external magnetic field H_{1n} via the electric quadrupole Q_{2m} . When a magnetic dipole $M_{1m'}$ is the primary order parameter in altermagnets, the dominant coupling is governed by $C_{1m';1n}^{2m}$. In this case, the induced quadrupole is proportional to $M_{1m'} H_{1n}$. As illustrated in the upper-left panel of Fig. 1, this leads to an odd (asymmetric) dependence of $Q_{x^2-y^2}$ on H_z in the low-magnetic field region. Under sufficiently strong magnetic fields, the Néel vector can be reoriented via the Dzyaloshinskii-Moriya interaction, leading to a reversal of the magnetic dipole-type altermagnetic order. In the higher field region, this reorientation of dipole order results in the symmetry dependence, which is the characteristic behavior of conventional magnetostriction in magnets.

In contrast, when the primary order parameter is a magnetic octupole $M_{3m'}$, the relevant coupling is determined by $C_{3m';1n}^{2m}$. Since the octupole does not transform as a dipole, its response to the magnetic field is fundamentally different. The induced quadrupole arises linearly from the product $M_{3m'} H_{1n}$ and changes sign under the reversal of the field or the magnetic octupole domain, as well as the Néel vector. As shown in the middle and lower panels of the left column, this produces an

odd (antisymmetric) linear dependence of $Q_{x^2-y^2}$ on H_z or H_x , which serves as a signature of octupolar (d -wave or g -wave) altermagnetic order. Thus, the parity of the piezomagnetic response directly reflects whether the underlying ferroic order is dipolar or octupolar.

We next discuss Eq. (5), which describes the induction of a magnetic dipole M_{1m} by symmetric strain σ_{2n} . This equation corresponds to the piezomagnetic effect given in Eq. (3). For magnetic dipole order, the coupling term $C_{1m';2n}^{1m}$ implies that strain modifies the dipole moment in a manner consistent with conventional magnetoelastic anisotropy. However, when a magnetic octupole $M_{3m'}$ is present, the term governed by $C_{3m';2n}^{1m}$ leads to a linear conversion of octupolar order into a magnetic dipole under strain, where symmetric strain $\sigma_{x^2-y^2}$ generates a finite magnetic dipole component (M_z or M_x) proportional to the pre-existing octupole. The induced magnetic dipole reverses sign when the strain or the octupole domain is reversed, reflecting the linear and symmetry-controlled nature of the coupling. In addition, weak ferromagnetic contributions arising from strain-induced Dzyaloshinskii–Moriya interactions may also appear in magnetization measurements.

Importantly, Fig. 1 demonstrates that the even or odd character of the response functions is not material-specific but is dictated by the angular-momentum addition rules expressed in Eqs. (4) and (5). The Clebsch-Gordan coefficients act as symmetry filters that determine which multipole combinations are allowed. Therefore, measurements of field- or strain-induced quadrupole and magnetization responses provide direct experimental access to the underlying ferroic multipole order and its tensorial structure in altermagnets.

X-ray Absorption Spectrum

X-ray absorption spectroscopy (XAS) is a powerful probe of electronic structure, providing element-specific and orbital-selective information on unoccupied states. In X-ray magnetic circular dichroism (XMCD), the difference between left- and right-circularly polarized absorption isolates rank-1 magnetic multipoles. The sum rules of XMCD have long provided a quantitative framework for extracting fundamental magnetic quantities, such as the spin angular momentum S_z , orbital angular momentum L_z , and the anisotropic magnetic dipole (AMD) T_z terms from core-level X-ray absorption spectra [50–53]. More recently, this framework has been reformulated using a complete electronic multipole basis, clarifying the symmetry content of XMCD and related dichroic signals [54]. Within this multipolar description, XAS dichroisms are understood as selective probes of electronic multipole moments with well-defined rank and parity. This reformulation unifies XMCD and XMLD within a common theoretical language and establishes core-level XAS as a powerful spectroscopic tool for identifying complex magnetic multipole order. Recent studies have revealed

that in altermagnets and noncollinear antiferromagnets, such as MnTe [55–57] and Mn₃Sn [58–60], the XMCD response is dominated not by conventional spin magnetization but by the AMD term [61–65], corresponding to $M_{1m}^{(1,1)}$. The ferroic ordering of AMD moments gives rise to finite XMCD signals and can induce ferromagnet-like anomalous Hall effects despite vanishing net magnetization [66, 67].

Complementary information is obtained from X-ray magnetic linear dichroism (XMLD), which is sensitive to rank-2 electric quadrupole moments. XMLD is defined as the difference in the XAS measured with orthogonal linear polarizations and can be classified into out-of-plane and in-plane components, depending on the polarization geometry. The out-of-plane XMLD, hereafter referred to as zXMLD, reflects the difference between polarizations parallel and perpendicular to a reference axis and primarily probes the spinless electric quadrupole $Q_{20}^{(\text{orb})} \propto (3z^2 - r^2)$, revealing orbital anisotropy and charge redistribution. In contrast, the in-plane XMLD (xyXMLD) measures the anisotropy within the basal plane and is governed by $Q_{22}^{(\text{orb})} + Q_{2-2}^{(\text{orb})} \propto (x^2 - y^2)$. Beyond these spinless contributions, XMLD also contains spinful components arising from magnetic dipole-dipole and dipole-octupole couplings, commonly denoted as P and R terms [54, 68, 69]. These higher-order multipoles encode anisotropic spin-quadrupole interactions and provide direct spectroscopic access to magnetocrystalline anisotropy and ferroic higher-rank magnetic order.

In this work, we apply XMCD and XMLD, interpreted based on the ferroic multipole order in the excited states, to a broad class of altermagnets and demonstrate that the XMCD and XMLD signals originate from piezomagnetic effects in d - and g -wave altermagnetic states. The resulting dichroic responses thus serve as clear spectroscopic signatures of strain-induced symmetry breaking. Furthermore, we show that inverse piezomagnetic effects can activate XMCD signals, establishing a unified picture in which XAS dichroisms selectively detect electronic multipoles and their coupling to lattice and magnetic degrees of freedom.

PIEZOMAGNETIC RESPONSE ON X-RAY ABSORPTION SPECTRA IN ALTERMAGNETS

To clarify the electronic structure and the piezomagnetic coupling in representative altermagnets, α -MnTe, MnF₂, and CrSb, we calculate the electronic ground state and dipole transitions in multi-electron systems, including full-multiplet effects. The electronic ground state calculations and XAS simulations were performed using the EDRIXS python modules [70]. The atomic model adopts the crystal-field parameters calculated from the crystal structure obtained from the CIF files in the materials project [71–73] and an effective magnetic field arising from the antiferromagnetic interaction that realizes the altermagnetic state.

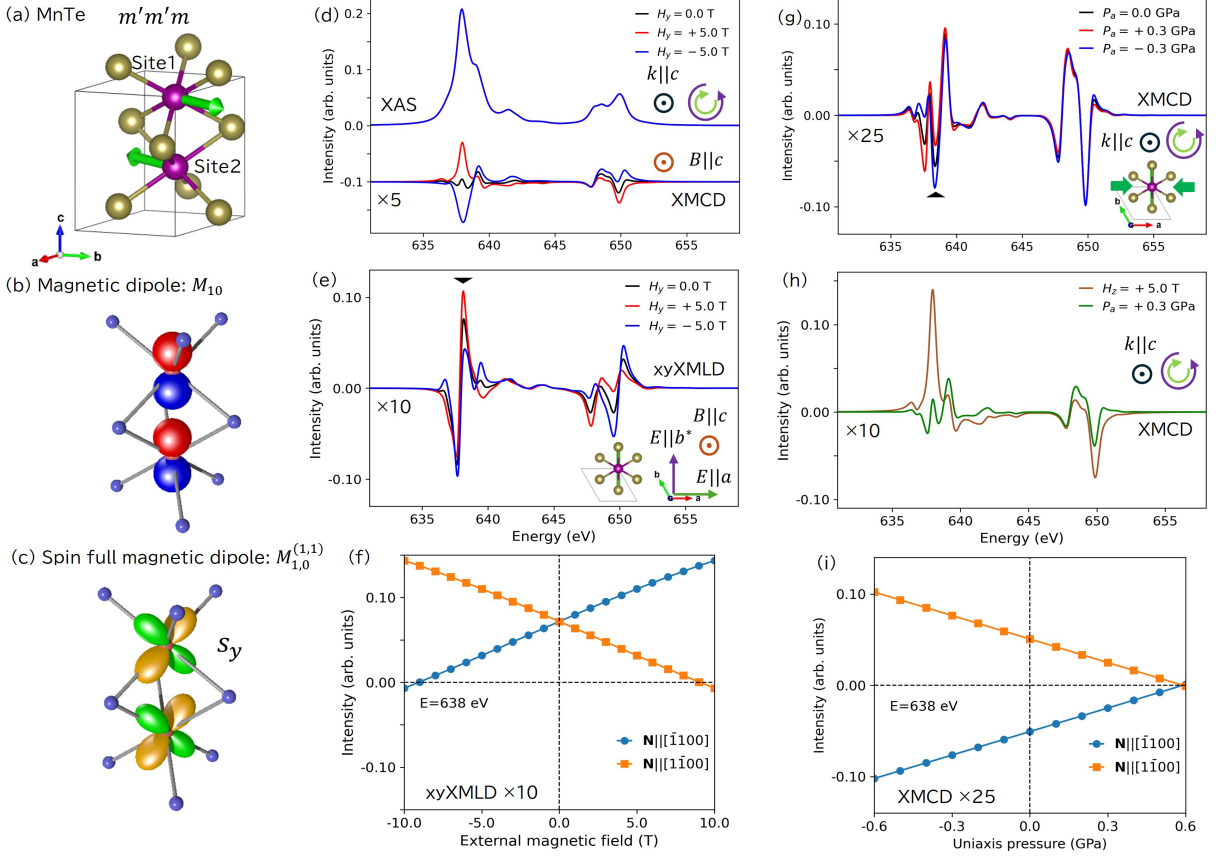


FIG. 2. Magnetic multipole structure and X-ray absorption spectra in α -MnTe. (a) Crystal and magnetic structure of α -MnTe with the NiAs-type lattice. The in-plane Néel vector is oriented along the $[1\bar{1}00]$ direction, described by the magnetic point group $mm'm'$. The green arrows represent the spin direction. This symmetry allows (b) a magnetic dipole M_{10} along the c -axis and (c) a spinful magnetic dipole $M_{10}^{(1,1)}$, whose microscopic distribution originates from the yz -type quadrupole moment associated with s_y spin component, where $x \parallel a$, $y \parallel b^*$, and $z \parallel c$. In the spherical-harmonic representation, red and blue colors denote the sign of the magnetic monopole charge density defined by $\mathbf{m} \cdot \mathbf{r}$, while green and yellow indicate the sign of the spin operator. (d) X-ray absorption spectrum (XAS) and X-ray magnetic circular dichroism (XMCD) spectra around the Mn L edge for magnetic fields applied parallel and antiparallel to the c -axis. (e) X-ray magnetic linear dichroism (xyXMLD) spectra measured between orthogonal linear polarizations $E \parallel a$ and $E \parallel b$ under opposite magnetic fields. (f) Magnetic-field dependence of the XMLD intensity at $E = 638$ eV. (g) XMCD spectra under uniaxial stress ($P_z = \pm 0.3$ GPa) applied perpendicular to the mirror plane. (h) Comparison between magnetic-field-induced and uniaxial-XMCD spectra. (i) Uniaxial-stress dependence of the XMCD intensity at $E = 638$ eV.

For the pressure response, the lattice strain induced by uniaxial pressure was estimated using the stiffness tensor obtained from the Materials Project database, and the corresponding change in the crystal field was evaluated.

g -wave altermagnet with Magnetic Dipole Symmetry

α -MnTe crystallizes in the NiAs-type structure, belonging to the hexagonal space group $P6_3/mmc$ (No. 194) [74–76]. Below the Néel temperature ($T_N \sim 310$ K [77]), MnTe exhibits a collinear antiferromagnetic order in which the Mn moments are aligned ferromagnetically within each ab plane and coupled antiferromagnetically between adjacent planes along the c -axis, as shown in Fig. 2(a). The Néel vector lies in the ab plane, typi-

cally along the $[1\bar{1}00]$ direction, lowering the symmetry to the magnetic point group $mm'm'$. This magnetic point group symmetry allows for a rank-1 magnetic dipole response M_{10} along the c direction [Fig. 2(b)], even though the net magnetization remains zero. This symmetry argument naturally explains the appearance of XMCD signals in α -MnTe despite its antiferromagnetic ground state. Microscopically, the XMCD signal originates from the spinful magnetic dipole operator $M_{10}^{(1,1)}$, whose spatial distribution corresponds to the s_y spin component coupled to the yz -type orbital character, as illustrated in Fig. 2(c). Such spin-quadrupole coupling manifests as a spin splitting associated with s_y in the band dispersion [78–80].

Figure 2(d) shows the calculated XAS and XMCD

spectra around the Mn L edge for incident X-rays parallel to the z axis ($[0001]$), obtained by exact diagonalization for the antiferromagnetic state of α -MnTe. Even in the absence of an external magnetic field, a finite XMCD signal appears due to the AMD term, which reflects the symmetry of the antiferromagnetic state. When a magnetic field is applied along the $[0001]$ direction, an additional XMCD component emerges from field-induced spin polarization. This contribution originates from a canting of the antiferromagnetic structure and reverses its sign upon reversing the magnetic field. In contrast, the XMCD component associated with the AMD term is governed by the orientation of the Néel vector and therefore does not reverse in the same manner. Under sufficiently strong magnetic fields, the Néel vector can be reoriented via the Dzyaloshinskii-Moriya interaction, leading to a reversal of the AMD-derived XMCD signal. This mechanism accounts for the reversal of the XMCD response observed in α -MnTe [55, 64].

When the Néel vector is aligned along $[\bar{1}100]$, the six-fold rotational symmetry of the crystal is reduced, giving rise to an xy -type X-ray magnetic linear dichroism (xyXMLD), a difference in XAS with polarization $E||x$ ($[1100]$) and $E||y$ ($[1\bar{1}20]$) [Fig. 2(e)]. The application of a magnetic field modifies the electronic states and induces a change in the XMLD intensity. In the low-field regime, where the Néel vector remains unchanged, the XMLD response is antisymmetric with respect to the magnetic field, reflecting the linear coupling between the field-induced spin canting and the electronic anisotropy. Figure 2(f) presents the magnetic-field dependence of the XMLD intensity at $E = 638$ eV. In the low-field region, the XMLD exhibits an antisymmetric dependence on the magnetic field, consistent with field-induced modifications through the linear piezomagnetic effect.

Figure 2(g) shows the change in the XMCD ($\mathbf{k}||[0001]$) spectrum induced by uniaxial stress applied perpendicular to the mirror plane. The applied strain lowers the symmetry and linearly couples to the underlying magnetic multipole order, thereby modulating the XMCD component. Figure 2(h) compares the XMCD spectra induced by a magnetic field and uniaxial stress. Since the microscopic origins are distinct, *i.e.*, field-induced spin canting in the former and strain-induced AMD in the latter, the spectral line shapes are different. Figure 2(i) presents the uniaxial-stress dependence of the XMCD intensity at $E = 638$ eV for the two Néel-vector orientations, $\mathbf{N} || [\bar{1}100]$ and $[1\bar{1}00]$. This leading-order linear and domain-sensitive behavior indicates that the XMCD response is symmetry-allowed to couple to the Néel vector through the piezomagnetic effect. The piezomagnetic effect observed in XMCD originates from the AMD term in the excited state, whereas in magnetization measurements, it is expected to manifest as weak ferromagnetism arising from a strain-induced Dzyaloshinskii-Moriya interaction.

d-wave altermagnet

MnF₂ adopts the rutile-type crystal structure belonging to the tetragonal space group $P4_2/mnm$ (No. 136) [81–83]. Below its Néel temperature ($T_N \sim 67$ K [84]), the Mn spins order collinearly along the c -axis in an antiferromagnetic configuration ($\mathbf{N} || [001]$), resulting in a magnetic symmetry described by the point group $4'/mmm'$ [Fig. 3(a)] [24]. This magnetic structure places MnF₂ in the class of *d*-wave altermagnets, where the staggered spin configuration gives rise to a d_{xy} -like momentum-dependent spin splitting in the s_z component [10–12]. The magnetic point group $4'/mmm'$ strictly forbids rank-1 magnetic dipole responses, ensuring that no net magnetization or dipolar XMCD signal appears in the absence of symmetry breaking. Notably, in the case of d_{xy} -like momentum-dependent spin splitting with $\mathbf{N} || [100]$, the magnetic point group is $m'mm'$, which allows XMCD along the b -axis [63]. On the other hand, the rank-3 magnetic octupole components $M_{3,\pm 2}$, corresponding to M_{xyz} or $M_{(x^2-y^2)z}$ -type distributions, are permitted in the *d*-wave rutile structure [Fig. 3(b)]. Since MnF₂ consists of two antiferromagnetically aligned sublattices, the spinless octupole $M_{3,\pm 2}^{(0,0)}$ does not form a ferroic order. Instead, the relevant ferroic order parameter is the spinful magnetic octupole $M_{3,\pm 2}^{(1,-1)}$, which combines the s_z spin component with a d_{xy} -type orbital distribution [Fig. 3(c)]. This spin-quadrupole entangled octupole provides the microscopic origin of magneto-optical responses in MnF₂ despite its zero net magnetization.

Figure 3(d) shows the calculated XAS and XMCD spectra around the Mn L edge for incident X-rays parallel to the c -axis. Consistent with symmetry, no intrinsic dipolar XMCD signal appears at zero magnetic field. When a magnetic field is applied along the c direction, a finite XMCD signal is induced through field-driven modulation of the spin component. This field-induced XMCD changes sign upon reversing the magnetic field, reflecting its odd parity with respect to the external field. Figure 3(e) presents the calculated xyXMLD spectra, which is the XAS difference between $E||[110](x)$ and $E||[\bar{1}10](y)$. In contrast to XMCD, the XMLD response directly probes the anisotropic electronic structure associated with the magnetic octupole order. The XMLD signal exhibits odd parity with respect to the magnetic field, indicating that it is sensitive to the sign of Néel vector. The magnetic-field dependence of the XMLD intensity at $E = 638$ eV is summarized in Fig. 3(f). The XMLD signal exhibits a leading-order linear dependence on the applied magnetic field and reverses sign between the two Néel-vector orientations ($\mathbf{N} || [001]$ and $[00\bar{1}]$), indicating a symmetry-allowed linear coupling between the field and the spinful magnetic octupole order parameter.

Figure 3(g) shows the XMCD spectra under uniaxial pressure applied along the in-plane direction. Although $4'/mmm'$ symmetry forbids dipolar responses, uniaxial strain $P||[110]$ lowers the symmetry and linearly cou-

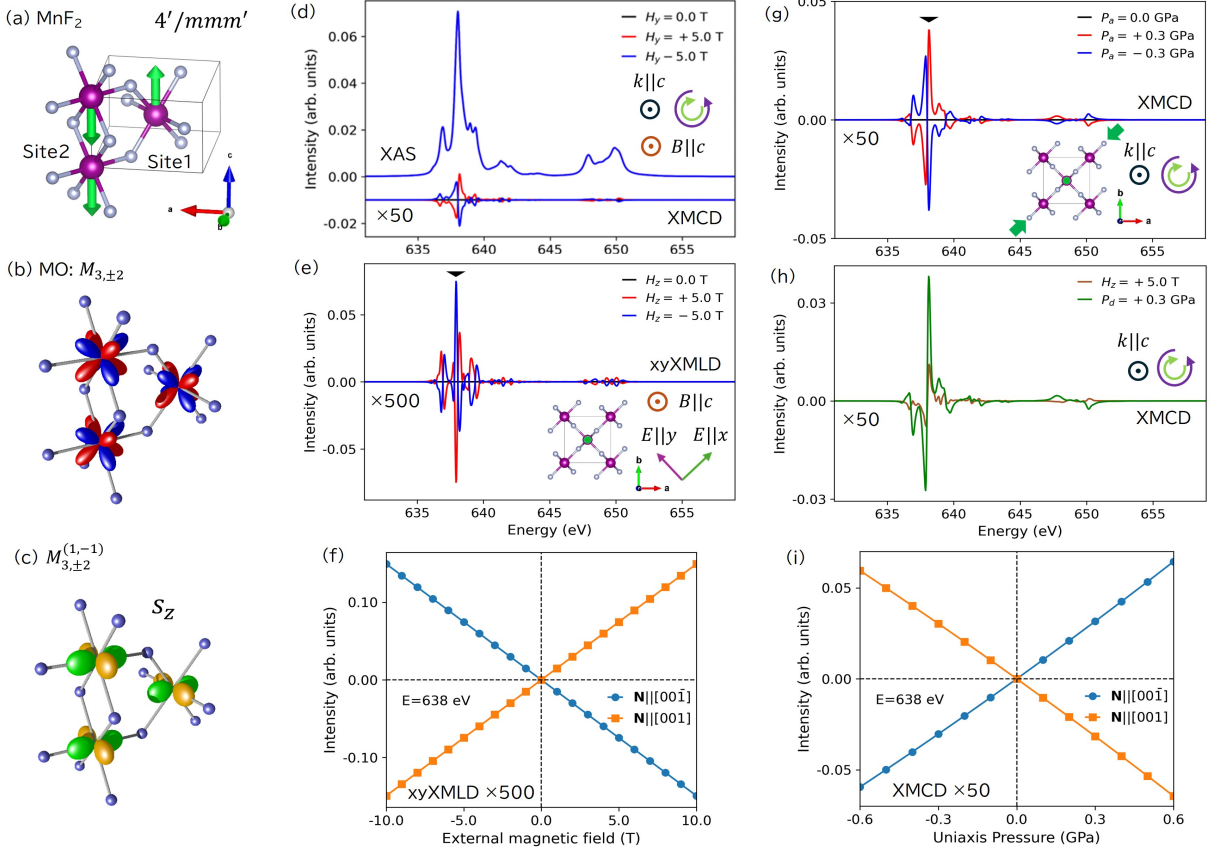


FIG. 3. Magnetic multipole structure and X-ray absorption spectra in MnF_2 . (a) Crystal and magnetic structure of MnF_2 with the rutile structure. The antiferromagnetic spins are aligned along the c -axis, reducing the symmetry to the magnetic point group $4'/mmm'$. This symmetry allows (b) the xyz -type magnetic octupole moments ($M_{3,\pm 2}$), and (c) their spinful counterpart of the xy -type quadrupole associated with the s_z spin component, $M_{3,\pm 2}^{(1,-1)}$, where $x \parallel a$, $y \parallel b$, and $z \parallel c$. (d) X-ray absorption spectrum (XAS) and X-ray magnetic circular dichroism (XMCD) spectra around the Mn L edge for magnetic fields applied parallel and antiparallel to the c -axis. (e) X-ray magnetic linear dichroism (xyXMLD) spectra measured between orthogonal linear polarizations ($E \parallel x$ and $E \parallel y$) under opposite magnetic fields. (f) Magnetic-field dependence of the XMLD intensity at $E = 638$ eV. The xyXMLD signal exhibits a linear dependence on the applied magnetic field and reverses sign depending on the Néel vector orientation ($\mathbf{N} \parallel [001]$ and $[00\bar{1}]$). (g) XMCD spectra under uniaxial pressure ($P_\sigma = \pm 0.3$ GPa). (h) Comparison between magnetic-field-induced and uniaxial-pressure-induced XMCD spectra. (i) Uniaxial-pressure dependence of the XMCD intensity at $E = 638$ eV.

ples to the magnetic octupole moment via piezomagnetic, thereby inducing a finite XMCD signal even without a magnetic field. The stress-induced XMCD reverses sign with the sign of the applied pressure, consistent with a linear piezomagnetic effect. Figure 3(h) compares the XMCD spectra induced by the magnetic field ($H \parallel c$) and by uniaxial pressure ($P \parallel [110]$). In MnF_2 , applying uniaxial stress along the $[110]$ direction lifts the degeneracy between sites 1 and 2 by generating an energy difference between them. As a result, the oppositely oriented spins at the two sites respond at different energies in the spectrum, leading to a finite XMCD signal. In contrast to MnTe , the magnetic dipole moments induced by the magnetic field and uniaxial pressure in MnF_2 are mainly from the conventional spin contribution. Both perturbations couple to identical spin channels; thus, the resulting XMCD spectral line shapes are similar. Fig. 3(i)

presents the uniaxial-pressure dependence of the XMCD intensity at $E = 638$ eV for the two Néel-vector orientations. The XMCD response exhibits a leading-order linear dependence on pressure and reverses sign between opposite antiferromagnetic domains.

This behavior demonstrates that strain provides a direct handle to control and detect the spinful magnetic octupole order in MnF_2 through the piezomagnetic effect.

g -wave altermagnet

CrSb shares the same NiAs-type crystal structure as α - MnTe , belonging to the hexagonal space group $P6_3/mmc$ (No. 194) [85, 86]. Below its Néel temperature ($T_N \sim 710$ K [87]), CrSb exhibits a collinear antiferromagnetic

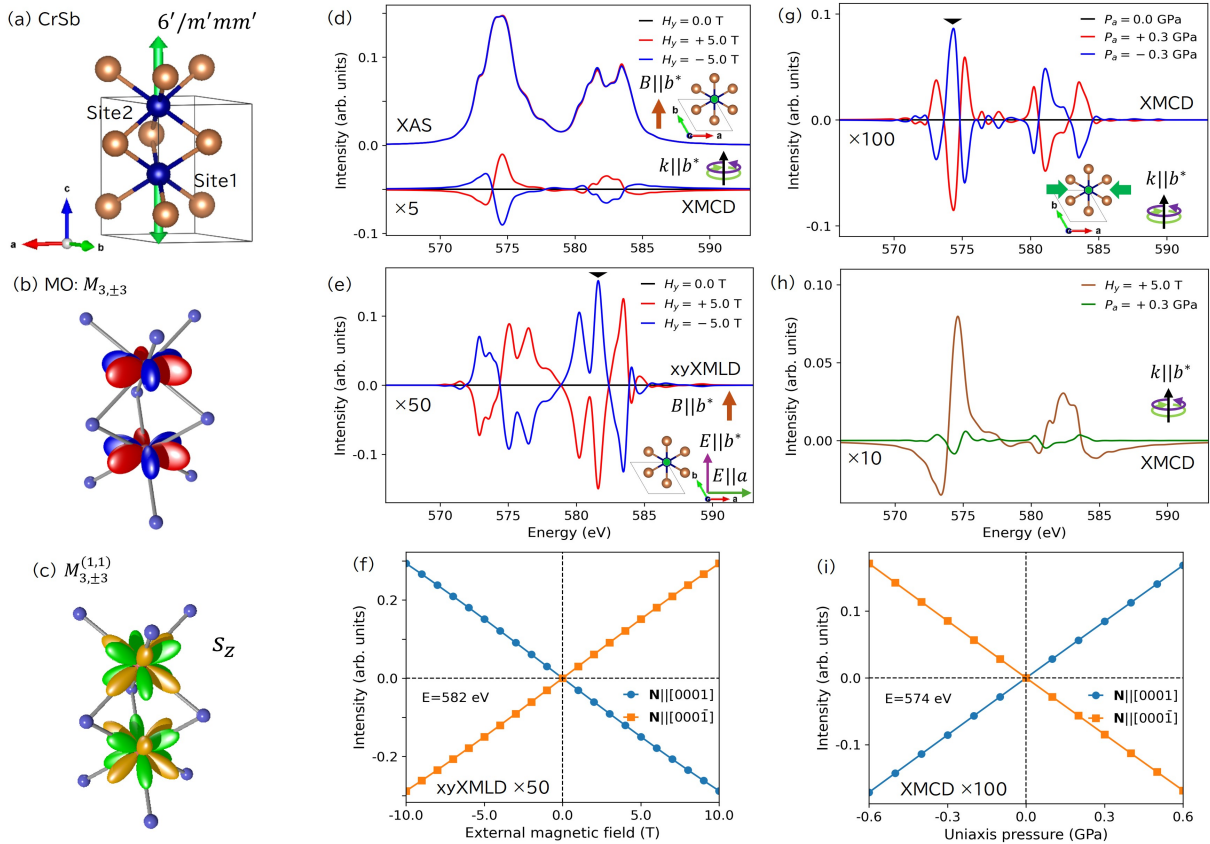


FIG. 4. Magnetic multipole structure and calculated X-ray absorption spectra in CrSb. (a) Crystal and magnetic structure of CrSb with the magnetic point group $6'/m'mm'$. This symmetry permits (b) the $(x^3 - 3xy^2)$ -like magnetic octupole moments ($M_{3,\pm 3}$) and (c) their spinful counterpart of the $z(x^3 - 3xy^2)$ -type hexadecapole associated with the s_z spin component, $M_{3,\pm 3}^{(1,1)}$, where $x \parallel a$, $y \parallel b^*$, and $z \parallel c$. (d) X-ray absorption spectrum (XAS) and X-ray magnetic circular dichroism (XMCD) spectra around the Cr L edge for magnetic fields applied parallel and antiparallel to the b^* direction. (e) X-ray magnetic linear dichroism (xyXMLD) spectra measured between orthogonal linear polarizations ($E \parallel a$ and $E \parallel b^*$) under opposite magnetic fields. The XMLD signal reverses its sign upon inversion of the magnetic multipole domain, demonstrating its odd response with respect to the external magnetic field. (f) Magnetic-field dependence of the xyXMLD intensity at $E = 582$ eV. The signal exhibits a linear dependence on the applied magnetic field and changes sign depending on the Néel vector orientation ($\mathbf{N} \parallel [0001]$ and $[000\bar{1}]$). (g) XMCD ($k \parallel b^*$) spectra under uniaxial pressure ($P_a = \pm 0.3$ GPa). The stress-induced XMCD emerges through piezomagnetic symmetry breaking even in the absence of net magnetization. (h) Comparison between magnetic-field-induced and uniaxial-pressure-induced XMCD spectra. (i) Uniaxial-pressure dependence of the XMCD intensity at $E = 574$ eV.

order in which the Cr spins are aligned along the c -axis [Fig. 4(a)]. This magnetic configuration gives rise to the magnetic point group $6'/m'mm'$, reflecting the rotation of the Néel vector from the ab plane in MnTe to the c -axis in CrSb. Under the $6'/m'mm'$ symmetry, rank-1 magnetic dipole responses along the c -axis are strictly forbidden, ensuring zero net magnetization and no intrinsic dipolar XMCD at zero field. However, higher-rank magnetic multipoles are symmetry allowed. In particular, the rank-3 magnetic octupole components $M_{3,\pm 3}$ are permitted [Fig. 4(b)]. The microscopic origin of these octupolar moments is described by the spinful operator $M_{3,\pm 3}^{(1,1)}$, which combines the s_z spin component with a $z(x^3 - 3xy^2)$ -type angular distribution [Fig. 4(c)].

Figure 4(d) shows the calculated XAS and XMCD spectra around the Cr L edge for incident X-rays with

$\mathbf{k} \parallel b^*$. Consistent with symmetry, no intrinsic dipolar XMCD appears at zero magnetic field. When a magnetic field is applied perpendicular to the c -axis, *e.g.*, along the b^* direction, XMCD signals emerge due to the canted spin components. The applied magnetic field gives rise to a reduction of the sixfold rotational symmetry, and thereby a finite xyXMLD (XAS difference between $E \parallel x$ [1100] and $E \parallel y$ [11 $\bar{2}$ 0]) signal emerges, as shown in Fig. 4(e). Although the appearance of XMLD under an in-plane magnetic field is expected from symmetry lowering, a key feature is that the XMLD response is odd with respect to the magnetic field. This behavior indicates that the electric quadrupole response is linearly coupled to the magnetic octupole moment through the external field, as depicted by Eq. (5), schematically expressed as a product of the magnetic octupole and the

magnetic field. Microscopically, the applied magnetic field modifies the relative stability of electronic states determined by the interplay between ligand-field anisotropy and spin orientation. As a result, field-induced redistribution of orbital occupations occurs, leading to a reversal of the XMLD sign. The underlying anisotropic electronic structure is closely related to that discussed for α -MnTe, *i.e.*, where the in-plane spin component modulates the spatial distribution of e_g^π orbitals. Figure 4(f) presents the magnetic-field dependence of the xyXMLD intensity at $E = 582$ eV. The signal exhibits a leading-order linear dependence on the magnetic field and reverses sign between the two Néel-vector orientations ($\mathbf{N} \parallel [0001]$ and $[000\bar{1}]$), demonstrating linear coupling between the magnetic field and the octupole order parameter.

Figure 4(g) shows the XMCD ($\mathbf{k} \parallel b^*$) spectra under uniaxial pressure applied in the basal plane without an external magnetic field. Even in the absence of a magnetic field, uniaxial pressure (P_a) lowers the crystal symmetry and couples linearly to the magnetic octupole moment via piezomagnetic interaction, thereby inducing a finite XMCD response along the b^* direction. The stress-induced XMCD reverses sign with the sign of the applied pressure, consistent with a linear piezomagnetic effect due to pre-existing magnetic octupole order.

Figure 4(h) compares the XMCD spectra induced by the magnetic field and uniaxial pressure. Since their microscopic origins differ, the spin component for the magnetic field and the AMD component from the magnetic octupole for strain, the spectral line shapes are distinct. Finally, Fig. 4(i) shows the uniaxial-pressure dependence of the XMCD intensity at $E = 574$ eV for the two opposite Néel-vector orientations. The leading-order linear and sign-reversing behavior suggests that strain can induce and probe the magnetic octupole order in CrSb, reflecting a symmetry-allowed coupling between magnetic octupole order and electric quadrupole responses in this g -wave altermagnet.

CONCLUSIONS

We have presented a symmetry-based framework for piezomagnetic and inverse piezomagnetic effects in alter-

magnets hosting ferroic magnetic dipole and octupole orders. By formulating the problem in the complete multipole basis, magnetic point groups can be systematically classified, and the allowed third-rank response tensors that connect magnetization, stress, magnetic field, and electric quadrupoles can be identified in a unified manner. This multipolar language provides a transparent criterion to distinguish dipolar, quadrupolar, and octupolar responses, even in systems with vanishing net magnetization. These couplings give rise to characteristic anisotropies and field/strain responses that serve as clear signatures of d - and g -wave altermagnets, also providing experimentally accessible fingerprints of hidden multipolar order. By combining symmetry analysis with element-specific XMCD and XMLD spectroscopy, our approach establishes a practical and material-specific strategy to detect and control ferroic magnetic dipole and octupole order in altermagnets. Since strain and magnetic field couple to the same underlying multipolar channels, magnetoelastic engineering offers a powerful route to manipulate antiferromagnetic domain states without relying on net magnetization. This framework thus opens a pathway toward strain-controllable spin functionalities and multipole-based device concepts that extend beyond conventional dipolar spintronics, highlighting altermagnets as a fertile platform for next-generation symmetry-driven spin phenomena.

ACKNOWLEDGMENTS

The authors thank M. Mizumaki, T. Uozumi, and T. Arima for constructive discussions. This project is partly supported by the Japan Society for the Promotion of Science (JSPS) KAKENHI (JP19H04399, JP24K03205, JP24H01685, and JP24K17603). This work was supported by the MEXT Quantum Leap Flagship Program (MEXT Q-LEAP) Grant Number JPMXS0118068681. This work is also partially supported by CREST(JPMJCR2435), Japan Science and Technology Agency (JST).

-
- [1] C. Kittel, *Introduction to Solid State Physics*, 8th ed. (Wiley, Hoboken, NJ, 2004).
 - [2] S. J. Blundell, *Magnetism in Condensed Matter* (Oxford University Press, Oxford, 2001).
 - [3] J. M. D. Coey, *Magnetism and Magnetic Materials* (Cambridge University Press, Cambridge, 2010).
 - [4] V. Baltz, A. Manchon, M. Tsoi, T. Moriyama, T. Ono, and Y. Tserkovnyak, *Reviews of Modern Physics* **90**, 015005 (2018).
 - [5] Y. Noda, K. Ohno, and S. Nakamura, *Phys. Chem. Chem. Phys.* **18**, 13294 (2016).
 - [6] T. Okugawa, K. Ohno, Y. Noda, and S. Nakamura, *Journal of Physics: Condensed Matter* **30**, 075502 (2018).
 - [7] K.-H. Ahn, A. Hariki, K.-W. Lee, and J. Kuneš, *Phys. Rev. B* **99**, 184432 (2019).
 - [8] M. Naka, S. Hayami, H. Kusunose, Y. Yanagi, Y. Motome, and H. Seo, *Nature Communications* **10** (2019).
 - [9] L. Šmejkal, R. Gonzalez-Hernandez, T. Jungwirth, and J. Sinova, *Sci. Adv.* **6**, eaba9399 (2020).
 - [10] L. Šmejkal, R. Gonzalez-Hernandez, T. Jungwirth, and J. Sinova, *Science* **375**, 70 (2022).

- [11] L. Šmejkal, J. Sinova, and T. Jungwirth, *Phys. Rev. X* **12**, 031042 (2022).
- [12] L. Šmejkal, T. Jungwirth, and J. Sinova, *Nat. Rev. Mater.* **8**, 653 (2023).
- [13] S. Hayami, Y. Yanagi, and H. Kusunose, *Journal of the Physical Society of Japan* **88**, 123702 (2019).
- [14] S. Nakatsuji, N. Kiyohara, and T. Higo, *Nature* **527**, 212 (2015).
- [15] M. Ikhlas, T. Tomita, T. Koretsune, M.-T. Suzuki, D. Nishio-Hamane, R. Arita, Y. Otani, and S. Nakatsuji, *Nature Physics* **13**, 1085 (2017).
- [16] T. Higo, H. Man, D. B. Gopman, L. Wu, T. Koretsune, O. M. van't Erve, Y. P. Kabanov, D. Rees, Y. Li, M.-T. Suzuki, *et al.*, *Nature photonics* **12**, 73 (2018).
- [17] O. J. Amin, A. D. Din, E. Golias, Y. Niu, A. Zakharov, S. C. Fromage, C. J. B. Fields, S. L. Heywood, R. B. Cousins, F. Maccherozzi, J. Krempaský, J. H. Dil, D. Kriegner, B. Kiraly, R. P. Campion, A. W. Rushforth, K. W. Edmonds, S. S. Dhesi, L. Šmejkal, T. Jungwirth, and P. Wadley, *Nature* **636**, 348 (2024).
- [18] S. Karube, T. Tanaka, D. Sugawara, N. Kadoguchi, M. Kohda, and J. Nitta, *Phys. Rev. Lett.* **129**, 137201 (2022).
- [19] H. Koizumi, Y. Yamasaki, and H. Yanagihara, *Nature Communications* **14**, 8074 (2023).
- [20] H. Koizumi and Y. Yamasaki, *Journal of Physics D: Applied Physics* **58**, 253002 (2025).
- [21] R. González-Hernández, L. Šmejkal, K. Výborný, Y. Yahagi, J. Sinova, T. c. v. Jungwirth, and J. Železný, *Phys. Rev. Lett.* **126**, 127701 (2021).
- [22] S. Hayami, *Phys. Rev. B* **109**, 214431 (2024).
- [23] S. Hayami, *Journal of Low Power Electronics and Applications* **14** (2024).
- [24] S. Bhowal and N. A. Spaldin, *Phys. Rev. X* **14**, 011019 (2024).
- [25] L.-D. Yuan, A. B. Georgescu, and J. M. Rondinelli, *Phys. Rev. Lett.* **133**, 216701 (2024).
- [26] K. D. Belashchenko, *Phys. Rev. Lett.* **134**, 086701 (2025).
- [27] M.-T. Suzuki, T. Koretsune, M. Ochi, and R. Arita, *Phys. Rev. B* **95**, 094406 (2017).
- [28] S. Hayami, M. Yatsushiro, Y. Yanagi, and H. Kusunose, *Phys. Rev. B* **98**, 165110 (2018).
- [29] M.-T. Suzuki, T. Nomoto, R. Arita, Y. Yanagi, S. Hayami, and H. Kusunose, *Phys. Rev. B* **99**, 174407 (2019).
- [30] H. Kusunose, R. Oiwa, and S. Hayami, *Journal of the Physical Society of Japan* **89**, 104704 (2020).
- [31] M. Yatsushiro, H. Kusunose, and S. Hayami, *Phys. Rev. B* **104**, 054412 (2021).
- [32] S. Hayami and H. Kusunose, *Journal of the Physical Society of Japan* **93**, 072001 (2024).
- [33] H. Kusunose, *Journal of the Physical Society of Japan* **77**, 064710 (2008).
- [34] Y. Kuramoto, H. Kusunose, and A. Kiss, *Journal of the Physical Society of Japan* **78**, 072001 (2009).
- [35] I. E. Dzyaloshinskii, *Soviet physics, JETP* **10**, 628 (1960).
- [36] A. S. Borovik-Romanov, *Soviet Physics JETP* **11**, 786 (1960).
- [37] A. S. Borovik-romanov, *Ferroelectrics* **162**, 153 (1994).
- [38] T. Aoyama and K. Ohgushi, *Phys. Rev. Mater.* **8**, L041402 (2024).
- [39] V. P. Andratskii and A. S. Borovik-Romanov, *Soviet Physics JETP* **24**, 687 (1967).
- [40] A. S. Prokhorov and E. G. Rudashevskii, *JETP Letters* **10**, 175 (1969).
- [41] J. Baruchel, A. Draperi, M. E. Kadiri, G. Fillion, M. Maeder, P. Molho, and J. L. Porteseil, *Journal de Physique Colloques* **49**, C8 (1988).
- [42] Y. Ogawa and S. Hayami, *Journal of the Physical Society of Japan* **94**, 063704 (2025).
- [43] V. T. N. Huyen, Y. Yanagi, and M.-T. Suzuki, *Phys. Rev. B* **112**, 104421 (2025).
- [44] V. T. N. Huyen, M.-T. Suzuki, K. Yamauchi, and T. Oguchi, *Phys. Rev. B* **100**, 094426 (2019).
- [45] E. Callen and H. B. Callen, *Phys. Rev.* **139**, A455 (1965).
- [46] E. Callen, *Journal of Applied Physics* **39**, 519 (1968).
- [47] Q. Meng, J. Dong, P. Nie, L. Xu, J. Wang, S. Jiang, H. Zuo, J. Zhang, X. Li, Z. Zhu, L. Balents, and K. Behnia, *Nature Communications* **15**, 6921 (2024).
- [48] M. Tomikawa, R. Araki, A. Ikeda, A. Nakamura, D. Aoki, K. Ishida, and S. Yonezawa, *Phys. Rev. B* **110**, L100408 (2024).
- [49] S. Hayami and H. Kusunose, *J. Phys. Soc. Jpn.* **93**, 072001 (2024).
- [50] B. T. Thole, P. Carra, F. Sette, and G. van der Laan, *Phys. Rev. Lett.* **68**, 1943 (1992).
- [51] P. Carra, B. T. Thole, M. Altarelli, and X. Wang, *Phys. Rev. Lett.* **70**, 694 (1993).
- [52] Y. Teramura, A. Tanaka, and T. Jo, *Journal of the Physical Society of Japan* **65**, 1053 (1996).
- [53] G. van der Laan and A. I. Figueroa, *Coord. Chem. Rev.* **277–278**, 95 (2014).
- [54] Y. Yamasaki, Y. Ishii, and N. Sasabe, *Science and Technology of Advanced Materials* **26**, 2513217 (2025).
- [55] A. Hariki, A. Dal Din, O. J. Amin, T. Yamaguchi, A. Badura, D. Kriegner, K. W. Edmonds, R. P. Campion, P. Wadley, D. Backes, L. S. I. Veiga, S. S. Dhesi, G. Springholz, L. Šmejkal, K. Výborný, T. Jungwirth, and J. Kuneš, *Phys. Rev. Lett.* **132**, 176701 (2024).
- [56] A. D. Din, O. J. Amin, P. Wadley, and K. W. Edmonds, *npj Spintronics* **2**, 25 (2024).
- [57] R. Yamamoto, L. A. Turnbull, M. Schmidt, J. C. Cor-saletti Filho, H. J. Binger, M. Di Pietro Martínez, M. Weigand, S. Finizio, Y. Prots, G. M. Ferguson, U. Vool, S. Wintz, and C. Donnelly, *Phys. Rev. Appl.* **24**, 034037 (2025).
- [58] M. Kimata, N. Sasabe, K. Kurita, Y. Yamasaki, C. Tabata, Y. Yokoyama, Y. Kotani, M. Ikhlas, T. Tomita, K. Amemiya, H. Nojiri, S. Nakatsuji, T. Koretsune, H. Nakao, T.-h. Arima, and T. Nakamura, *Nat. Commu.* **12**, 5582 (2021).
- [59] S. Sakamoto, T. Higo, M. Shiga, K. Amemiya, S. Nakatsuji, and S. Miwa, *Physical Review B* **104**, 134431 (2021).
- [60] S. Sakamoto, T. Higo, Y. Kotani, H. Kosaki, T. Nakamura, S. Nakatsuji, and S. Miwa, *Physical Review B* **110**, L060412 (2024).
- [61] Y. Yamasaki, H. Nakao, and T.-h. Arima, *Journal of the Physical Society of Japan* **89**, 083703 (2020).
- [62] N. Sasabe, M. Kimata, and T. Nakamura, *Phys. Rev. Lett.* **126**, 157402 (2021).
- [63] N. Sasabe, M. Mizumaki, T. Uozumi, and Y. Yamasaki, *Physical Review Letters* **131**, 216501 (2023).
- [64] N. Sasabe, Y. Ishii, and Y. Yamasaki, *Phys. Rev. B* **112**, 224401 (2025).
- [65] Y. Ishii, N. Sasabe, and Y. Yamasaki, *Altermagnetic xmed in hematite distinct from weak ferromagnetic contributions* (2026), arXiv:2603.00442 [cond-mat.str-el].

- [66] S. Hayami and H. Kusunose, Phys. Rev. B **103**, L180407 (2021).
- [67] S. Ohgata and S. Hayami, Phys. Rev. B **112**, 014421 (2025).
- [68] P. Carra, H. König, B. Thole, and M. Altarelli, Physica B: Condensed Matter **192**, 182 (1993).
- [69] G. van der Laan, Physical review letters **82**, 640 (1999).
- [70] Y. Wang, G. Fabbris, M. Dean, and G. Kotliar, Computer Physics Communications **243**, 151 (2019).
- [71] K. Persson, Materials data on mnfe (sg:194) by materials project (2016), an optional note.
- [72] K. Persson, Materials data on mnf2 (sg:136) by materials project (2014), an optional note.
- [73] K. Persson, Materials data on crsb (sg:194) by materials project (2015), an optional note.
- [74] S. Greenwald, Acta Crystallographica **6**, 396 (1953).
- [75] T. Komatsubara, M. Murakami, and E. Hirahara, Journal of the Physical Society of Japan **18**, 356 (1963).
- [76] N. Kunitomi, Y. Hamaguchi, and S. Anzai, Journal de Physique **25**, 568 (1964).
- [77] K. Walther, Solid State Communications **5**, 399 (1967).
- [78] I. I. Mazin, Phys. Rev. B **107**, L100418 (2023).
- [79] T. Osumi, S. Souma, T. Aoyama, K. Yamauchi, A. Honma, K. Nakayama, T. Takahashi, K. Ohgushi, and T. Sato, Phys. Rev. B **109**, 115102 (2024).
- [80] Z. Liu, M. Ozeki, S. Asai, S. Itoh, and T. Masuda, Phys. Rev. Lett. **133**, 156702 (2024).
- [81] M. Griffel and J. W. Stout, Journal of the American Chemical Society **72**, 4351 (1950).
- [82] C. G. Shull, W. A. Strauser, and E. O. Wollan, Phys. Rev. **83**, 333 (1951).
- [83] Z. Yamani, Z. Tun, and D. H. Ryan, Canadian Journal of Physics **88**, 771 (2010).
- [84] J. W. Stout and H. E. Adams, Journal of the American Chemical Society **64**, 1535 (1942).
- [85] B. T. M. Willis, Acta Crystallographica **6**, 425 (1953).
- [86] H. Nagasaki, I. Wakabayashi, and S. Minomura, Journal of Physics and Chemistry of Solids **30**, 2405 (1969).
- [87] T. Hirone, S. Maeda, I. Tsubokawa, and N. Tsuya, Journal of the Physical Society of Japan **11**, 1083 (1956).